2002-06

Low-altitude infrared propagation in a coastal zone: refraction and scattering

Doss-Hammel, Stephen M.

Low-altitude infrared propagation in a coastal zone: refraction and scattering

Stephen M. Doss-Hammel, Carl R. Zeisse, Amalia E. Barrios, Gerrit de Leeuw, Marcel Moerman, Arie N. de Jong, Paul A. Frederickson, and Kenneth L. Davidson

Midwave and long-wave infrared propagation were measured in the marine atmosphere close to the surface of the ocean. Data were collected near San Diego Bay for two weeks in November 1996 over a 15-km horizontal path. The data are interpreted in terms of effects expected from molecules, aerosol particles, and refraction. Aerosol particles are a dominant influence in this coastal zone. They induce a diurnal variation in transmission as their character changes with regular changes in wind direction. A refractive propagation factor calculation is introduced, and it is systematically applied to the model and to the data analysis. It is shown that this refractive propagation factor is a necessary component of a complete near-sea-surface infrared transmission model.

OCIS codes: 010.1300, 010.1320, 010.1110, 010.4030, 010.1310, 290.4020.

1. Introduction

Infrared signals propagating along extended horizontal paths near the sea surface are frequently distorted by strong vertical fluxes of momentum and heat. Along such paths the propagation conditions are complex. Large aerosol particles, which are quite efficient at scattering and absorbing infrared waves, may be found in great quantities close to the sea surface, providing an important extinction mechanism in addition to the extinction from molecules.[1–3] Refractive effects (for example, the formation of a mirage) are frequently encountered along low-altitude horizontal paths in coastal environments.

We report here on one of a series of experiments performed during 1996–1997 on Zuniga Shoals just outside San Diego Bay. We found that infrared propagation in this region near the coast was strongly influenced by aerosol particles. Diurnal variations in wind direction introduced diurnal changes in transmission. When the wind came from the sea, during the day, it brought relatively clean air over the path, accompanied by high transmission. When the wind came from the land, during the night, it brought aerosol particles made up of dust, pollution, and surf spray over the path, reducing the transmission.

In this paper the equation for the infrared signal σ is written as

$$\sigma = \tau_m \tau_p F^2 \equiv \tau F^2, \tag{1}$$

where τ_m and τ_p represent the transmission that is due to extinction by absorption and scattering by molecules and aerosol particles, respectively. Their product is denoted by τ and simply called the transmission. The refractive propagation factor F (a term borrowed from radio wave propagation theory) represents refractive effects. The refractive propagation factor is defined to be the ratio of the electric field received under prevailing refractive conditions to the electric field that would have been received in free space.[4] The signal is normalized to one at its free-space value.

There are two basic results presented in this analysis. First, aerosol effects and in particular the diurnal variation in aerosol have a strong influence on infrared propagation. Second, the propagation factor F is also an important determinant of signal intensity. The primary determinant of this factor is the air–sea temperature difference.

S. M. Doss-Hammel (hammel@spawar.navy.mil), C. R. Zeisse, and A. E. Barrios are with the Atmospheric Propagation Branch of the Space and Naval Warfare Systems Center D858, 49170 Propagation Path, San Diego, California 92152-7385. G. de Leeuw, M. Moerman, and A. N. de Jong are with the TNO Physics and Electronic Laboratory, P.O. Box 96864, 2509 JG The Hague, The Netherlands. P. A. Frederickson and K. L. Davidson are with the Department of Meteorology, 589 Dyer Road, Room 254, Naval Postgraduate School, Monterey, California 93943-5114.

Received 9 August 2001; revised manuscript received 31 January 2002.

0003-6935/02/183706-19$15.00/0

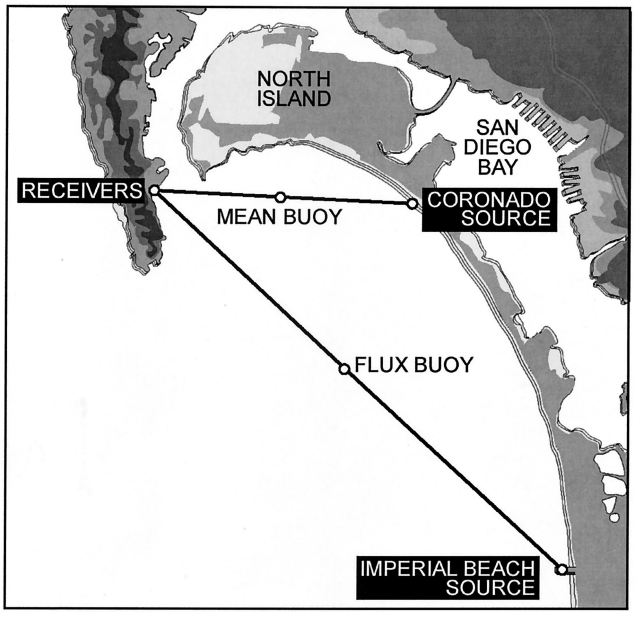

Fig. 1. Overhead view of Zuniga Shoals just outside San Diego Bay showing two low-altitude paths used to measure infrared propagation during November 1996. The short path was 7 km long and the long path was 15 km long.

2. Experiment

The experiment ran for several weeks during November of 1996. It was part of the experimental series[5] called Electro-Optical Propagation Assessment in Coastal Environments (EOPACE). Transmission, aerosol, and meteorological measuring systems were set up across the ocean at Zuniga Shoals just outside San Diego Bay. We report here on those data obtained between 6 November (day 311 of that year) and 21 November (day 326) when all systems were operating simultaneously.[6] This particular experiment in the EOPACE series was chosen for a detailed analysis because of its unusual weather: For the first week there was a strong Santa Ana condition during which hot dry air was blown across the sea; for the second week the normal weather pattern for this region was reestablished and cool sea air from the northwest flowed across the shoals.

Figure 1 shows an overhead view of the experimental area. There were two infrared propagation paths. The longer 15-km path began with a source mounted outside the surf zone on a pier in Imperial Beach, California, and ended with a receiver at the Naval Submarine Base, Pt. Loma. The shorter 7-km path began with a transmitter on the beach of the Naval Amphibious Base, Coronado, and also ended with a receiver at the Naval Submarine Base, Pt. Loma. The paths were nominally horizontal and close to the surface of the ocean; they were so close that the tide, whose amplitude is approximately 1 m in this locale, substantially altered the path altitude throughout the day. The propagation paths necessarily included small (less than 100 m) segments over land. The paths also passed over a jetty and approximately 100 m of sheltered water at the entrance to San Diego Harbor. Navy ships and small boats sailing in and out of the harbor often blocked these paths causing the signal to drop momentarily to zero.

Continuous meteorological measurements were obtained from buoys anchored near the middle of each path. A buoy measuring meteorological fluxes (the flux buoy) was anchored near the middle of the long path. Another buoy measuring mean meteorological parameters (the mean buoy) was anchored near the middle of the short path. Aerosol particle size distributions were measured continuously on the pier at Imperial Beach. The aerosol counter at Imperial Beach was close to the infrared transmitter and over the ocean beyond the surf line so that, when the wind came from the land, air containing continental aerosol particles and surf spray entered the counter. Radon radioactivity[7] was measured continuously at the Naval Submarine Base.

The aerosol measurements at Imperial Beach were crucial for the analysis of these propagation data. The aerosol counters suffered a 28-h power failure between days 319.74 and 320.91. No data from this time period are included in our analysis.

A. Transmission Equipment

TNO Physics and Electronic Laboratory (TNO-FEL) operated the transmissometer on the long path. The transmitter contained a blackbody whose aperture was located in the focal plane of a Newtonian telescope. The receiver contained an identical telescope with a discrete (nonimaging) detector in its focal plane. The blackbody radiance was chopped with a blade, and a reference signal from the blade was transmitted by radio to a synchronous detector (also called a lock-in detector) at the receiver. Optical filters mounted in front of each detector determined the spectral bands. These filters plus the rather gradual spectral dependencies of source radiance and detector response determined the overall spectral responsivities shown in Figs. 2 and 3.

The transmissometer was absolutely calibrated[8,9] by a careful series of laboratory and field measurements. During the field calibration measurements the complete chain of detector (Graseby), filter, optics of receiver and transmitter, source plus modulator, reference signal, preamplifier, lock-in amplifier (EG&G), and data-acquisition board (a LabMaster PCL 860) were used over a test range of 800 m ($\pm$ 1 m) in well-defined, stable (cloudy) weather conditions. For these conditions the MODTRAN propagation model was run, and the measured signal level was set to the predictions from the model. During the laboratory measurements, the individual components were tested: The detector responsivity was checked with a standard 900 K source, the spectral transmission of the filters was measured, as was the transmission of the optics of the receiver and the transmitter. The optical blur circle was determined to be 1 mrad. Also, the radiance of the source was measured, and the homogeneity of the responsivity over the detector sensitive area was checked. Finally, the detector position relative to the optical fo-

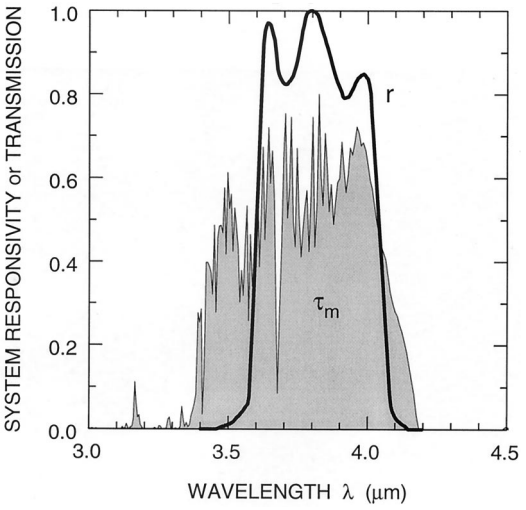

Fig. 2. System responsivity (curve r) in the midwave band for the long-path transmissometer. The curve was normalized to unity at its maximum. This curve is the product of the spectral radiance of the source, the spectral transmission of the filter, and the spectral responsivity of the detector. The shaded area represents the transmission of an aerosol-free atmosphere calculated by MODTRAN 3.5 for a temperature of 20°C, an absolute humidity of 10 g m^{-3}, and a range of 15 km.

cus was checked, and the alignment telescopes were boresighted with the optical axis of the primary measurement optics. These procedures were carried out before and after each trial to investigate possible reduction in transmission of the optical chain because of weather influences.

The midwave and long-wave detectors were alternately placed in the focal plane of the receiver primary to record data from each of these bands with a single receiving telescope. Each detector remained in the receiver for several hours at a time, which consequently produced the data toggle between the bands; there is no occasion when data from both bands are simultaneously available. The most important parameters of the long-path instrument are listed in Table 1.

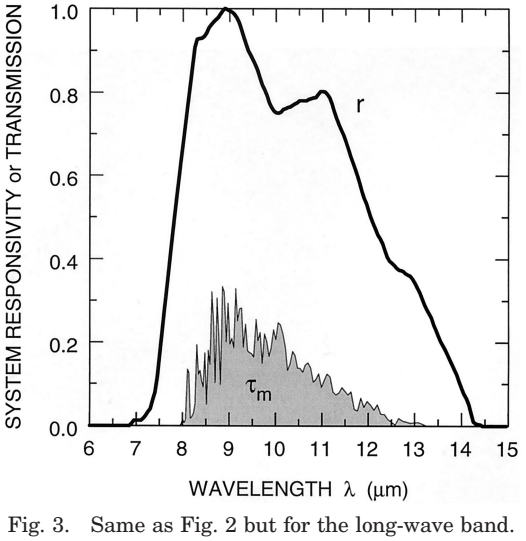

Fig. 3. Same as Fig. 2 but for the long-wave band.

Table 1. Transmissometer Characteristics[a]

Quantity	Value	Units
Primary mirrors		
Focal length	0.4	m
Diameter	0.2	m
F-number	*F*/2	—
Transmitter		
Blackbody temperature	1100	K
Field of view (full angle)	6.25	mrad
Chopping frequency	820	Hz
Altitude above mean sea level	9.0	m
Receiver		
Detector		
Size (square)	2	mm
Midwave material	InSb	—
Midwave detectivity	3×10^{11}	cm $Hz^{-1/2}$ W^{-1}
Long-wave material	HgCdTe	—
Long-wave detectivity	4.7×10^{10}	cm $Hz^{-1/2}$ W^{-1}
Filter half-power wavelengths		
Midwave	3.60–4.04	μm
Long wave	7.82–12.05	μm
Field of view (full angle)	5	mrad
Altitude above mean sea level	5.4	m
Path		
Range	15006	m
Bearing[b]	141.1	° true
Altitude above mean sea level	2.8	m
Noise to Free-Space Signal Ratio		
Equivalent noise bandwidth	0.05	Hz
Midwave	<0.67	%
Long wave	<0.17	%
Accuracy	±20	%

[a]The path altitude is the midpath value for free space (straight rays and a curved Earth).
[b]T_x, transmitter; R_x, direction of transmitter from receiver.

The Space and Naval Warfare Systems Center operated another transmissometer on the short path. Unfortunately, the short-path receivers (one for each band) had a field of view (0.8-mrad full angle) that was too small for coastal operation. If the optical spot were initially centered on the detector in these receivers, any angular change greater than 0.4 mrad was sufficient to move the spot off of the detector. A relatively large change in air temperature (approximately 4–5°C) would be required to produce this angular change when the air is cooler than the sea, as it is a majority of the time[10] out in the ocean well away from the coast. But a change of only 1°C would be required when the air is warmer than the sea and there is little wind.[11] During the first part of our experiment, Santa Ana conditions advected hot air from the land out over the water, and the air temperature often increased during the day to become as much as 10°C warmer than the sea temperature. Under these conditions refractive wander of the spot required frequent optical realignment during the day and left numerous gaps in the data during the night when the equipment was unattended. After analy-

Table 2. Buoy Meteorology Instruments and their Mounting Heights (m)

Instrument	Measurement	Flux Buoy
RM Young	Mean wind speed and direction	3.80
Rotronics	Air temperature, relative humidity	3.86
Thermistor	Sea temperature	−1.17
Barometer	Atmospheric pressure	0.22
TCM compass	Buoy magnetic heading	0.25

Table 4. Geographical Coordinates of Platforms Used in the November 1996 Field Experiment at Zuniga Shoals

	North Latitude 32°		West Longitude 117°	
Platform	Minutes	Seconds	Minutes	Seconds
Transmitter	34	46.2	8	5.7
Receiver	41	4	14	7.4
Flux buoy	37	40	11	0

sis, the short-path data were found to contain the same trends as the long-path data except that refractive effects were almost completely absent from the data because of the small field of view of the instrument. Consequently, no further mention will be made of the short-path transmission data in this paper.

B. Meteorological Buoy

A meteorological flux buoy (anchored near the middle of the long path) was deployed during this experiment. This buoy has flux and motion sensors in addition to sensors to measure mean meteorological parameters and sea surface temperature. Table 2 gives the type of each instrument and the height at which it was mounted on the buoy. Table 3 shows the mean value, standard deviation, and extreme values for observations made at the flux buoy. The coordinates of the buoy and the long-path transmitter and receiver are given in Table 4.

C. Aerosol Equipment

At the end of the long path, aerosol particle counters[12] were installed on the deck of the lifeguard station on Imperial Beach Pier. They were mounted 9 m above mean sea level. These instruments counted particles whose diameters ranged from 0.2 to 47 μm. We reiterate that the particle counters on the pier were on the ocean side of the surf zone. When the wind blew from the ocean to the land, particle sizes were characteristic of the open ocean. When the wind blew from the land to the ocean, particle sizes were characteristic of surf spray and continental sources together. The influence of the surf was determined in separate experiments that simultaneously employed two or more aerosol counters, one on land and another at sea. These measurements[13–15] showed that surf could locally increase the aerosol concentration by 1–2 orders of magnitude. We employed only one aerosol counter at sea with the result that we were incapable of separating these two components. However, we do distinguish between the two aerosol types, and the procedure used to separate the types, and assign appropriate refractive indices, is described in subsection 5.C.

3. Meteorological Synopsis

Figure 4 shows meteorological data obtained at the flux buoy during the experiment. The meteorological conditions in the Zuniga Shoals area during the experiment consisted of three regimes:

1. During days 311–318 high pressure to the northeast brought continental air into the area, and a weak large-scale pressure gradient forcing allowed a strong diurnal land–sea breeze to dominate Zuniga Shoals. The presence of a continental-influenced air mass led to large temperature and humidity variations over Zuniga Shoals as the wind shifted from onshore during the day to offshore at night.
2. During days 319–321 a passing low-pressure system to the north strengthened the large-scale pressure gradient in the region, leading to more persistent winds. The tail end of a cold front passed Zuniga Shoals on day 320 (during the power outage at Imperial Beach). The stronger large-scale forcing was dominant over the local land–sea breeze circulation, and the temperature and humidity variations over Zuniga Shoals were small during this period.
3. During days 322–326 a high-pressure center to the southwest brought maritime-influenced air to the region, and a weakened pressure gradient allowed the diurnal land–sea breeze to return. However, the presence of a marine air mass led to smaller variations in temperature and humidity over Zuniga Shoals than during days 311–318, and conditions were generally more cool and moist.

The different nature of the first and last regimes can be most clearly seen in Fig. 4(i) showing the air–sea temperature difference as a function of time.

Table 3. Statistics for Meteorological Measurements (1994 Observations) Made at the Flux Buoy at the Long-Path Midpoint

Variable	T_{air}	T_{sea}	$T_{air} - T_{sea}$	U	P	Q	W_s	W_d
Unit	°C	°C	°C	%	hPa	g m^{-3}	m s^{-1}	deg
μ (mean value)	17.0	16.7	0.30	70.4	1016.4	10.5	2.94	195
σ (standard deviation)	2.4	0.3	2.37	16.3	3.2	2.0	1.55	110
Minimum value	12.2	16.1	−4.5	12	1008	2.9	0.00	0
Maximum value	28.0	17.6	11.2	99	1023	15.1	7.1	360

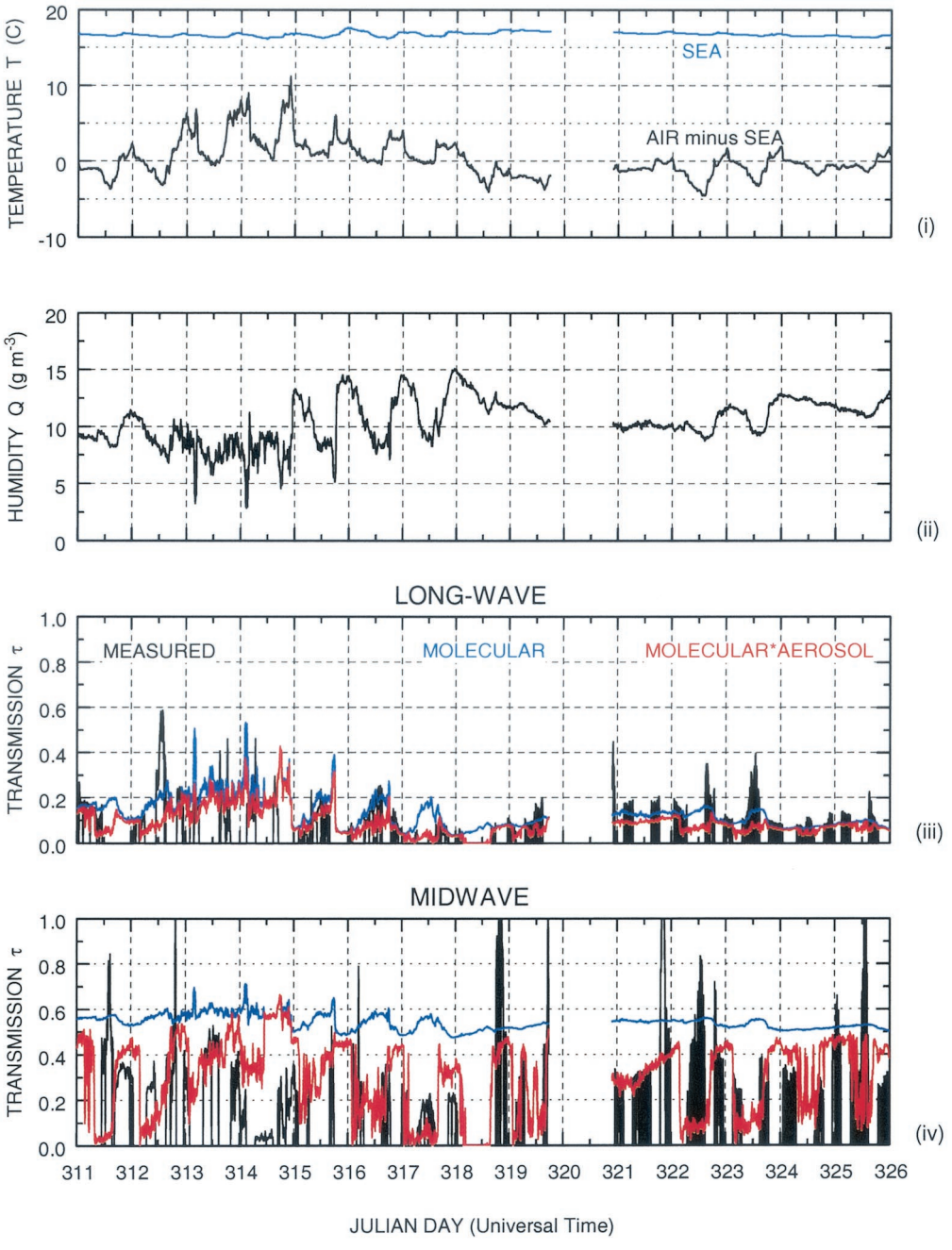

Fig. 4. Meteorological data, observed signal, and calculated transmission for the entire experimental period. No data were included, nor calculations made, for day 320 because of a failure of the aerosol particle counters during that interval. The upper two panels show meteorological data recorded at the flux buoy. The bottom two panels show how the measured signal (black curve) compares with the transmission calculated for clear air (blue curve) and for air containing aerosol particles (red curve).

No precipitation was observed at the North Island Naval Air Station (located on Coronado just to the north of the short propagation path) during the entire experiment, except for light and short-lived drizzle at 320.04 and rain at 324.71. Fog, mist, and haze were observed at North Island intermittently from the latter half of day 317–319 and on day 324.

4. Data Example

Three days of typical meteorological and propagation data are shown in Figs. 5 and 6, respectively. The first two days, 316 and 317, were during the first regime that included the Santa Ana with strong diurnal variations under the influence of the large pressure gradient. A transition to the second synoptic regime began on day 318. The propagation data are for the midwave band. The shaded regions in each panel represent local nighttime. The upper panel in Fig. 5 shows a diurnal variation in the wind direction that is most evident on days 316 and 317. During the day the wind came from the direction 270°, from the west and the sea. During the night (except for

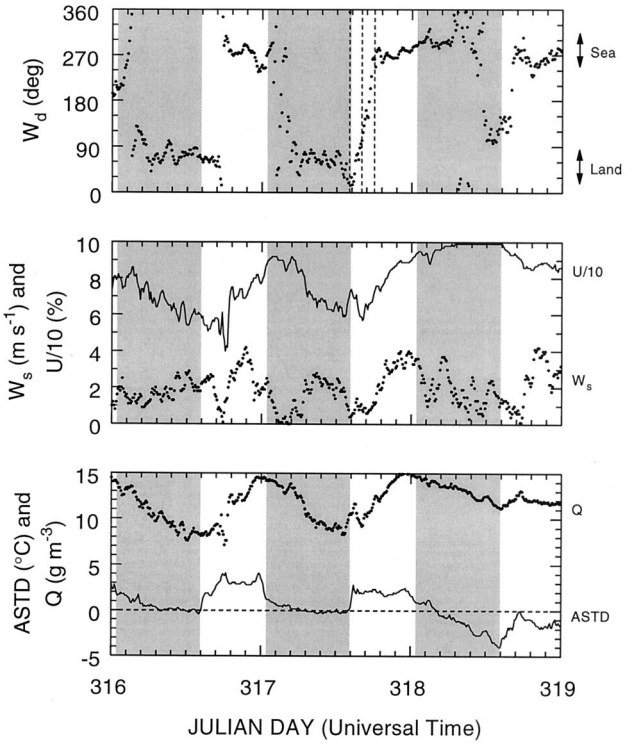

Fig. 5. Three days of meteorological data measured at the flux buoy at the center of the long propagation path. Q is the absolute humidity and $T_{air} - T_{sea}$ is the air–sea temperature difference (ASTD). The light and shaded bands indicate local day and night, respectively. (Each shaded band begins at local sunset and ends at local sunrise.) The upper panel shows how the wind tended to come from the land during the night and from the sea during the day. The middle panel shows a period of constant (99%) relative humidity from 318.3 to 318.5 when there was fog. The three dashed vertical lines in the upper panel show when the aerosol data in Figs. 8 and 9 were measured.

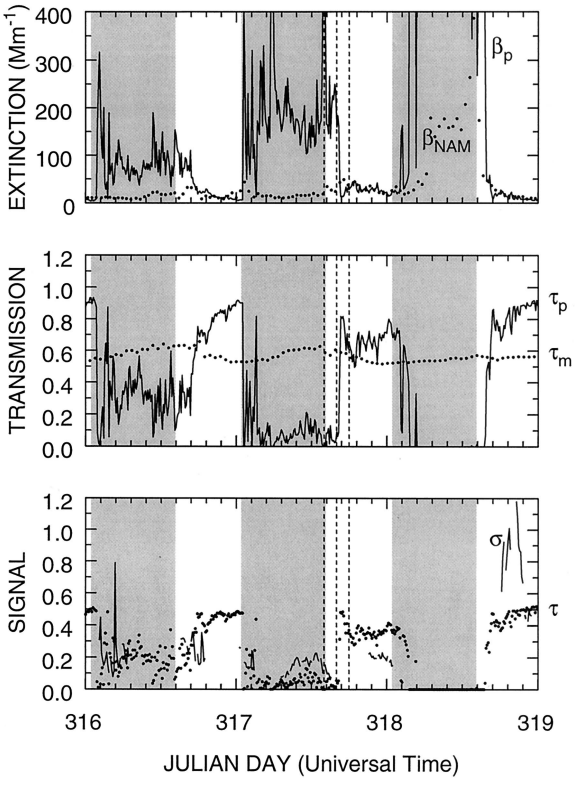

Fig. 6. Transmission and signal data in the midwave band for the three days shown in Fig. 5. Upper panel: curve, extinction at 4.0 μm calculated from aerosol number distributions measured at the Imperial Beach Pier; dots, extinction at 4.0 μm predicted by the Navy Aerosol Model (NAM). Middle panel: curve, aerosol transmission corresponding to the curve in the upper panel; dots, molecular transmission calculated by MODTRAN for the responsivity given by the solid curve in Fig 2. Bottom panel: dots, product of the two transmission values shown in the middle panel; curve, measured signal. The dashed vertical lines have the same meaning as in Fig. 5. A signal of 1.0 corresponds to the free-space signal.

the night of day 318) the wind came from the direction 60°, from the northeast and the land. The transition between these two directions could be abrupt (as it was at 316.7) or gradual (as it was between 317.6 and 317.8). Transitions were accompanied by low wind speeds (see, for example, the period between 317.1 and 317.2); then the winds were light and variable.

During the last part of the third night, between 318.3 and 318.6, the relative humidity reached a high value (the data record shows a value of 99%) and remained constant. Fog was visually observed at North Island Naval Air Station during this period. The bottom panel in Fig. 5 shows how the absolute humidity fell with air temperature throughout the night while the relative humidity stayed constant. (Only the air–sea temperature difference is shown in this panel. However, the sea temperature remained relatively constant throughout the experiment at 16.7 ± 0.3°C according to Table 3.)

Figure 6 shows, by the curve in the upper panel, the aerosol extinction at 4.0 μm derived from observed particle size distributions by calculations described in Section 5. The dots in this panel show the aerosol extinction derived from the Navy Aerosol Model. During the day (unshaded regions) the wind came from the sea, and there was good agreement between the model and the field data. During the night (shaded regions) the wind came from the land, and there was poor agreement between them.

The middle panel in Fig. 6 shows the aerosol transmission calculated with Beer's law from the extinction in the upper panel and the molecular transmission calculated by MODTRAN by use of the responsivity given by the solid curve in Fig. 2. A range of 15 km was used for each of these calculations. The molecular transmission can be seen to remain relatively constant because it is not sensitive to changes in humidity in the midwave band. However, the aerosol transmission shows a strong diurnal variation. The aerosol transmission drops to zero during the fog.

The lower panel in Fig. 6 shows how the measured data (curve) compare with the calculated transmission (dots). Although the signal measurements do not show as much diurnal variation as we would

expect from the aerosol contribution to the transmission, there is modest agreement (to within approximately a factor of 2) between the observed signal and the computed transmission. At 318.85 the measured signal exceeds the free-space value.

5. Transmission Analysis

The fundamental assumption for the analysis was that the entire experimental region was horizontally homogeneous. Molecular (clear-air) transmission was derived from MODTRAN[16,17] calculations based on the data obtained at the midpath (flux) buoy. Mie theory[18] and Beer's law were used to derive the aerosol transmission from particle size distributions obtained at the Imperial Beach Pier. Data from the flux buoy were also used to derive vertical refractivity gradients from which the refractive propagation factor was calculated. Finally the product of these three calculations was compared with the signal measurement.

All data were averaged over 10-min intervals. The various computers recording these data were synchronized only to within several minutes; data whose intervals overlapped one another were assumed to be simultaneous and received the same time stamp.

A. Horizontal Homogeneity

Of course the assumption of homogeneity is untrue. There were variations in relative humidity along the path, and these variations altered the particle size distributions and thus the extinction coefficients. However, for relative humidity lower than approximately 90%, a relatively small humidity variation will not drastically alter the extinction coefficient. Another substantial effect is the vertical dispersion of the particles produced by the surf. At Imperial Beach the particle size distributions were measured close to the surf where the particles are more concentrated than they are at larger fetches out along the actual transmission paths. A transport model[19] would be required to account for the decrease of particle concentration with fetch, but the application of such a model is outside the scope of the present analysis. Furthermore, the surf itself is an inhomogeneous source that fluctuates on short time scales and varies spatially along the coast. The aerosol averaging time of 10 min reduces the temporal fluctuations to some extent.

For the meteorological parameters, similar considerations and reservations apply, although the physics is not as complicated as for the aerosols. The nearby land produces gradients in temperature, humidity, and wind speed, especially in offshore winds. Indeed, we did observe strong gradients in point measurements of air temperature at the beginning, middle, and end of the path. For example, during the Santa Ana, temperatures at the path endpoints differed by 7°C. The wind direction can vary appreciably in this topographically complicated locale over and above the sea breeze effect. Furthermore, measurements made from a small boat indicated water temperature fluctuations of up to 3°C along the path.

Spatial inhomogeneities are inherent in a coastal environment. Large differences along the paths have been observed, and at this point we do not know of any way to account for them in detail. The results show that the infrared signal is reasonably well explained when we account for the effects of aerosol particles, molecules, and refraction derived from measurements made at a single point.

B. Molecular Analysis

Molecular transmission was calculated with version 3.5 of MODTRAN.[16,17] Inputs to the calculation were observations of pressure, air temperature, and relative humidity at the flux buoy. The calculation was performed for a horizontal path. Aerosol particles were not introduced; it was a clear-air calculation. We chose a model atmosphere containing concentrations of ozone, methane, nitrogen dioxide, and carbon monoxide corresponding to the mid-latitude winter default atmosphere in MODTRAN. All other gases corresponded to the 1976 U.S. Standard Atmosphere default atmosphere.

We introduced the instrument responsivities $r(\lambda)$ shown for each band in Figs. 2 and 3 by using a shell that operated on the standard MODTRAN output file. The output file contained the spectral molecular transmission values $\tau_m(\lambda, L)$. The shell, which also contained the spectral radiance of the source $N(\lambda)$, performed the integration

$$\tau_m = \frac{\int N(\lambda)\tau_m(\lambda, L)r(\lambda)\mathrm{d}\lambda}{\int N(\lambda)r(\lambda)\mathrm{d}\lambda} \tag{2}$$

to provide a band-averaged molecular transmission τ_m for each band.

Figure 7 shows the clear-air transmission calculated by MODTRAN for our instrument. The primary dependence is on absolute humidity. There is a secondary dependence on air temperature, and there is a small dependence (not shown in Fig. 7) on pressure. Figure 7 shows that extinction by water vapor is smaller in the midwave band than in the long-wave band. For an absolute humidity corresponding to the mean ± 1 standard deviation (as observed at the flux buoy), the molecular transmission is 0.12 ± 0.07 in the long-wave band and 0.55 ± 0.035 in the midwave band.

It is difficult to assign an absolute accuracy to this calculation. Even if MODTRAN were an accurate model of the transmission of well-controlled gaseous samples, it would certainly be a less accurate model of the transmission of an uncontrolled atmosphere such as that above Zuniga Shoals. In the phenomenon of radar ducting it has been shown[20] that radar propagation models are quite accurate provided that the atmospheric conditions determining the duct are accurately known. In a real atmosphere, however,

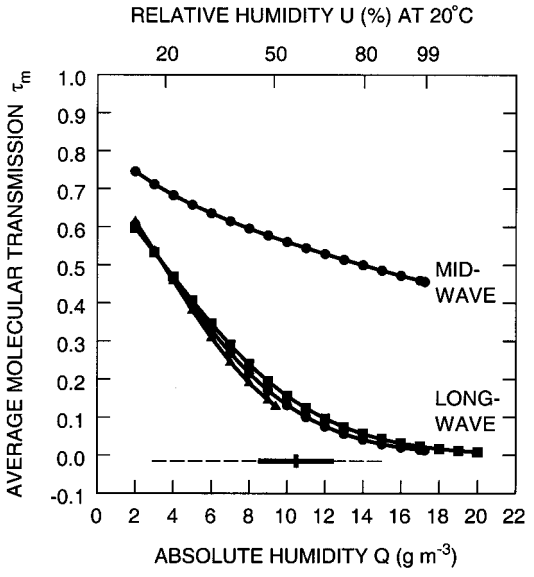

Fig. 7. Broadband molecular transmission as a function of absolute humidity for a 15-km path. These curves were calculated with MODTRAN 3.5 for the responsivities shown in Figs. 2 and 3. Data for a temperature of 10°C are shown by triangles, data for a temperature of 20°C are shown by circles, and data for a temperature of 30°C are shown by squares. (No temperature dependence is shown for the midwave band because all three curves would closely overlap the one shown for 20°C.) Ranges of absolute humidity observed at the flux buoy during the experiment are indicated just above the x axis: The vertical tick is at the mean, the solid curve spans the mean ± 1 standard deviation, and the dashed line spans the minimum to maximum.

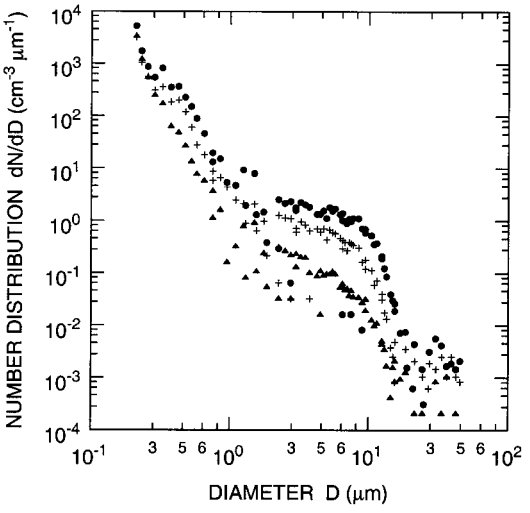

Fig. 8. Aerosol number distributions measured at the Imperial Beach Pier for three different times during day 317 (12 November 1996). The circles are for 1400 UT, the plus signs are for 1600 UT, and the triangles are for 1800 UT. The vertical dashed lines in Figs. 5 and 6 also indicate these three times. Beyond approximately 30 μm the data become quite noisy because of the poor counting statistics: Over a 10-min period the counter may capture only one or two particles of such large diameter.

such knowledge is usually impossible. We assume that our situation is similar and that our largest error is determined by our inability to accurately specify the atmospheric conditions.

C. Aerosol Analysis

The settings appropriate to each particle counter were used to convert raw counts to a numerical size distribution dN/dD (cm^{-3} μm^{-1}), where dN is the number of particles per cubic centimeter, having a diameter between D and $D + dD$. Three such measured size distributions are shown in Fig. 8. They were recorded at 2-h intervals when the wind direction changed from 60° and 270°, coming initially from the land (circles) and finally from the sea (triangles). In the diameter range of several micrometers, the number of particles per cubic centimeter drops by roughly an order of magnitude as the wind changes direction from offshore to onshore. This is contrary to the expectation if these particles are assumed to be sea spray particles with a sole source over the sea. However, a dominant local source for sea spray aerosol is the surf zone where such amounts of sea spray aerosol are produced that locally the concentrations are enhanced by 1–2 orders of magnitude. In this case an offshore wind advects aerosol from a local source located at the land–sea transition, through the aerosol sampling point and the entire transmission path.

Curves were fit to the raw data before further analysis. Polynomials of degree 2 (a Junge distribution) and 5 were used for the fit. For each 10-min measurement the data themselves were replaced by the fifth-order polynomial within the range of diameters actually obtained during that measurement. Outside that range the data were extrapolated to a diameter of 0.01 μm with a log-normal distribution and to a diameter of 32 μm with the Junge distribution.

The rationale for this extrapolation is as follows. Particles smaller than the minimum measured diameter of 0.2 μm usually do not contribute to the infrared extinction unless many of those small particles are present. At the other end of the size range, however, particles make a significant contribution to the infrared extinction. For example, measurements[21] made with Rotorod impaction devices with good counting statistics (resulting from a large sample volume) indicate that the inclusion of large particles in the Mie calculation makes a significant difference in the derived optical properties. This was found to be especially true in high winds that produce many large sea spray particles. However, large particles are normally found in small amounts. Therefore, with the aerosol counters used during the EOPACE experiment, it may take an impractically long time to obtain reasonable statistics for these large particles. By extrapolating to a diameter of 32 μm, we are able to take into account the influential large particles while maintaining a reasonable integration time during the measurement.

The role played in the extrapolation by the minimum and maximum particle sizes has been studied.[22] The choice of 32 μm as an upper limit is reasonable and has been adopted as a standard procedure by

TNO-FEL. Particles larger than this are rarely counted with the equipment used in the current experiments in spite of the instrumental upper limit of 47 μm mentioned above.

To summarize, optical parameters were calculated with Mie theory[18] from curves that were fit to the measured size distributions. The calculation always spanned the same diameter interval, namely, $(D_1, D_2) = (0.01, 32)$ μm. This had the further advantage of minimizing errors that were due to incomplete sampling caused, for example, by rejection of a count when a statistically insufficient number of particles was obtained in a given size interval.

We calculated the particle extinction β_p (Mm^{-1}) at an optical wavelength λ (μm) by integrating the product of the particle concentration and the Mie efficiency factor for extinction over all particle sizes:

$$\beta_p(\lambda) = \int_{D_1}^{D_2} a Q_{\mathrm{ext}}(D, \lambda, \tilde{n}) \frac{\mathrm{d}N}{\mathrm{d}D} \mathrm{d}D. \tag{3}$$

The dimensionless Mie efficiency factor is defined as

$$Q_{\mathrm{ext}}(D, \lambda, \tilde{n}) \equiv \frac{\Delta}{a}. \tag{4}$$

Here Δ ($\mu\mathrm{m}^2$) is the optical crosssection of a single particle for extinction as given by Mie theory, $\tilde{n}$ is the complex refractive index of that particle, and

$$a \equiv \frac{\pi}{4} D^2 \tag{5}$$

is the physical cross-sectional area ($\mu\mathrm{m}^2$) of the particle.

A refractive index must be supplied to calculate the Mie efficiency factor. In providing this index, we assumed the measured size distribution to consist of a mixture of dry continental particles with one index[23] and sea spray particles with another index. The index for sea spray was composed by means of interpolating with respect to relative humidity between the index for dry sea salt[24] and the index for water.[25] Measured distributions were separated into the two particle types and a separate version of Eq. (3) with the appropriate index used for each type. The separation was carried out as follows.[26] Particles smaller than 0.4 μm in diameter were assumed to be entirely continental in origin, and particles larger than 0.4 μm in diameter were assumed to be a mixture of both types. Furthermore, on the basis of frequent observations that the size distribution of continental aerosols in the relevant size range can be approximately described by a power-law distribution (Junge, 1952), the contribution of the continental particles to the total measured concentrations of particles larger than 0.4 μm was determined from extrapolation of a power-law distribution fitted to the measured concentrations of particles smaller than 0.4 μm. The amplitude of this power-law distribution is determined by the concentrations of the smallest particles, and the slope was determined by a fit to the variation of these concentrations with the particle diameter. Subtraction of the concentrations of the continental particles from the total measured concentrations yielded the concentrations of the sea spray particles with diameters between 0.4 and 32 μm.

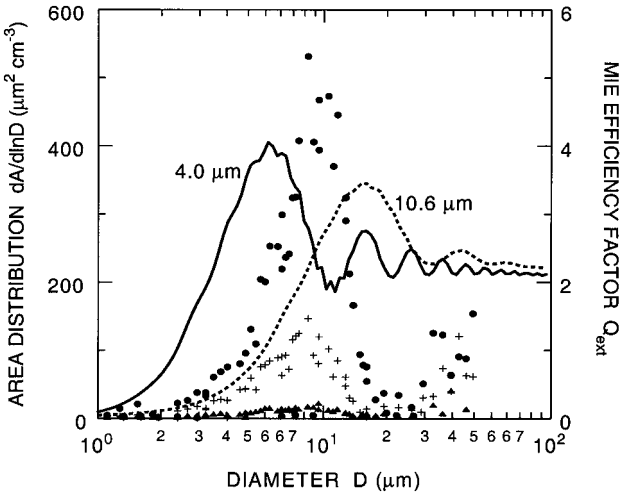

Fig. 9. Symbols show the data of Fig. 8 presented as an area distribution (left ordinate). The curves show Mie efficiency factors for extinction (right ordinate). Solid curve, Mie factor at a wavelength of 4.0 μm for an aerosol particle with a complex refractive index of $(1.448) - i(0.002194)$. Dashed curve, Mie factor at a wavelength of 10.6 μm for an aerosol particle with a complex refractive index of $(1.444) - i(0.0716)$. The extinction coefficient for each wavelength is proportional to the area under the product of a Mie efficiency factor for that wavelength and a particle area distribution.

To convert extinction to transmission at range L (Mm), Beer's law was used:

$$\tau_p = \exp[-\beta_p(\lambda) L]. \tag{6}$$

The optical wavelengths chosen for the midwave and long-wave bands were 4.0 and 10.6 μm, respectively.

The integration stipulated by Eq. (3) is easier to visualize if the number distribution in Eq. (3) is converted to a distribution of area $A \equiv Na$:

$$\beta_p(\lambda) = \int_{D_1}^{D_2} Q_{\mathrm{ext}}(D, \lambda, \tilde{n}) \frac{\mathrm{d}A}{\mathrm{d} \ln D} \mathrm{d} \ln D. \tag{7}$$

In Eq. (7) $\mathrm{d}A$ ($\mu\mathrm{m}^2\ \mathrm{cm}^{-3}$) is the total physical cross-sectional area, per unit volume, of particles having a diameter between D and $D + \mathrm{d}D$. If total areas are distributed with respect to $\ln D$ instead of D and then plotted with respect to $\ln D$, equal areas in the resultant plot will represent equal physical cross-sectional areas per unit volume in the sample. Figure 9 shows the data of Fig. 8 replotted in terms of area distributions. Also shown in Fig. 9 are the Mie efficiency factors for the midwave and long-wave bands. The area under the product of one of the efficiency curves with one of the area distributions yields aerosol extinction. With the aid of Fig. 9 it is easy to see how, in this particular example, the wind

Table 5. Error Estimates for the Analysis[a]

Parameter	Uncertainty	Predictor	Midwave Error	Long-Wave Error
Q	± 1.7 g m^{-3}	τ_m	± 0.03 at 0.55	± 0.05 at 0.14
β_p	$\pm$ factor of 2	τ_p	$+0.26$ to -0.39 at 0.58	$+0.19$ to -0.36 at 0.69
T_{air} T_{sea}	± 1.2°C, ± 0.6°C	F^2	$+0.37$ to -0.08 at 0.98	
—	—	σ	$+0.60$ to -0.68 at 0.31	$+0.59$ to -0.64 at 0.09

[a]Uncertainties in the parameters shown in the first column lead to the errors in the last two columns for the predictor. The errors are evaluated at the mean value of the predictor. The last row gives the root sum square of the errors in the first three rows.

direction strongly influences the aerosol extinction in each of the infrared bands.

In our opinion, the largest error in the aerosol analysis is the inaccuracy of the particle counters themselves. In an experiment[27] at San Nicolas Island, 11 particle counters similar to the ones used here were operated for 11 days along with a variety of other instruments (such as transmissometers and visioceilometers) that measure optical extinction that is due to aerosol particles. The particle concentration at any given diameter was observed to differ by up to an order of magnitude among these 11 instruments. However, differences in concentration are smoothed during the integration described by Eq. (3), and the extinction derived from the 11 instruments "agreed within a factor of two to three"[27] with the other measurement methods. Assuming a factor of 2 and translating from extinction to transmission with Beer's law [Eq. (6)], this means that

$$\tau_p{}^2 \leq \tau_p \leq \sqrt{\tau_p}. \tag{8}$$

Taking the mean value of τ_p (0.69 in the long wave and 0.58 in the midwave) in these limits, we arrive at the error estimates shown in the second line of Table 5.

6. Transmission Results

The results of the transmission calculation are shown in Fig. 4. Important observations from Fig. 4 are as follows:

1. The molecular transmission (blue curve) in the midwave band [panel (iv)] is more constant than it is in the long-wave band [blue curve in panel (iii)]. This result has been discussed previously in connection with Fig. 7.
2. The blue curves in panels (iii) and (iv) consistently show the opposite trend to the time series shown in panel (ii): Molecular transmission is primarily a decreasing monotonic function of absolute humidity.
3. The red curves in panels (iii) and (iv) are usually closer to the black curves than are the blue curves, confirming the expectation that a calculation based on extinction by particles and molecules is a better estimator of the observations than a calculation based on molecular extinction alone.
4. The black curve in panel (iv) closely follows the trend of the red curve. This means that the midwave measurements are dominated by aerosol extinction.
5. In panels (iii) and (iv) there are times [for example, at day 312.5 in panel (iii) and at day 322.5 in panel (iv)] when the black curve significantly exceeds the red curve. There are even times [for example, at day 318.75 in panel (iv)] when the black curve appears to go above free space (a transmission of 1.0). In these cases the transmission model is a poor predictor of the measured signal.

With regard to the last point, part of the midwave data for day 318 is shown on an expanded time scale in Fig. 10. The measured signal is above the calculated clear-air transmission for a period of approximately 3.5 h and approaches twice the clear-air calculation (and 120% of the free-space value) at its maximum. Scattering and absorption cannot be responsible for these signal levels because these effects can only reduce the signal. In the remainder of this paper we examine the hypothesis that refraction can explain such effects.

7. Refractive Analysis

To study refractive effects in infrared propagation, the optical refractive conditions along the path must be known. A meteorological model must be used to derive optical refractivity from the meteorological conditions measured during the experiment. Then

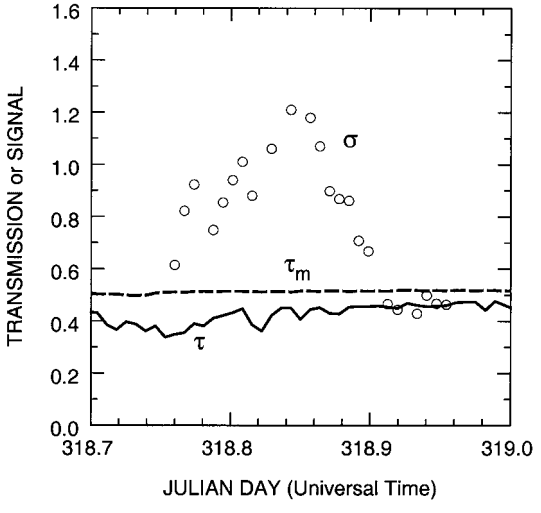

Fig. 10. Observations of signal (open circles) compared with calculations of transmission (solid curve) during part of day 318. The calculated clear-air transmission is shown as the dashed line.

Table 6. Statistics of the Analysis[a]

Band	Data	N	ε_{rms}	ε_{std}	μ	σ	β	ρ
Long wave	Obs.	706	—	—	0.143	0.087	—	1.00
	τ_m	706	0.080	0.080	0.135	0.066	0.008	0.48
	τ	706	0.101	0.086	0.090	0.049	0.053	0.39
	σ	551	0.076	0.070	0.115	0.074	0.028	0.66
Midwave	Obs.	782	—	—	0.331	0.220	—	1.00
	τ_m	782	0.315	0.227	0.549	0.036	−0.218	−0.12
	τ	782	0.275	0.275	0.317	0.165	0.014	0.00
	σ	587	0.232	0.226	0.387	0.241	−0.056	0.49

[a]Observed signal statistics are given in the rows labeled Obs. Statistics for several comparisons are shown as τ_m for observation versus clear-air transmission, τ for observation versus transmission, and σ for observation versus signal. N is the number of comparisons, ε is the error, μ is the mean value, σ is the standard deviation, β is the bias, and ρ is the correlation coefficient.

a propagation model is required to calculate refractive effects for a given vertical refractivity profile. We now describe these models.

A. Meteorological Model

Vertical refractivity profiles were obtained for the long path from bulk measurements made at the midpath flux buoy, and these profiles were assumed to be constant in range for each time period. We thus used the fundamental assumption, discussed above in subsection 5.A, that refractive conditions were homogeneous along the path.

Following the definition for radio-wave-modified refractivity, we define modified optical refractivity M as

$$M(z) = N(z) + 0.157z, \tag{9}$$

where N is the optical refractivity [$N = (n - 1) \times 10^6$ where n is the refractive index] and z is the height in meters. The second term in Eq. (9) is used to account for Earth curvature. Unlike the radio wave case in which refractivity has a strong dependence on humidity, humidity is not an important factor for infrared and optical frequencies, and the refractivity is formulated by use of air pressure and temperature only:

$$N = 77.6 \frac{P}{T_{air}}. \tag{10}$$

Here, the pressure P is specified in hectopascals and the temperature T_{air} is in degrees Kelvin. There is also a term[28] that was omitted from Eq. (10) that depends on the optical wavelength; however, this term is small and acts only as an additive constant in each wave band. Because refractive effects depend only on the vertical gradient of the refractive index, this additional term contributes nothing to the propagation effects. Therefore we assumed in our analysis that modified optical refractivity is independent of wavelength.

We used the well-known Liu, Katsaros, and Businger (LKB)[29] meteorological model to compute vertical refractivity profiles from bulk measurements of temperature and pressure. As mentioned in Section 3, during Santa Ana conditions in the first part of the observation period we experienced stable conditions when the air–sea temperature difference ($T_{\mathrm{air}} - T_{\mathrm{sea}}$) became as high as +10°C. These high positive values of air–sea temperature difference, combined with the low wind speeds that were also observed, were outside the limits of the LKB model. (In fact, we know of no duct model in the literature that can adequately handle these high values of air–sea temperature difference in combination with low wind speeds.) When the LKB model would not converge, the scaling parameters for the stability function could not be determined. Therefore we could not produce a refractivity profile, and we omitted any refractive analysis for these time periods. This reduced the number of comparisons that could be made between calculated and observed signals by 22% in the longwave band and 25% in the midwave band. (Please refer to the column labeled N in Table 6.)

B. Refractive Propagation Model

The ray optics model can be used to calculate the refractive propagation factor F. As we noted above we borrowed the term propagation factor from the radar propagation community. It is more accurate to define F as the refractive propagation factor because we use the term in a restricted way: Changes in field amplitude that are due to refractive effects are included, but changes that are due to any reflection of the propagating beam are not included.

We assumed horizontal homogeneity of the refractive field: The only gradients in refractive index occur in the vertical coordinate. The assumption of horizontal homogeneity means that the computation of the ray trace can be confined to a vertical plane. The analysis is performed in this two-dimensional plane, and we define a coordinate system based at the receiver. The local coordinate system is further transformed to bring the curved surface of mean sea level to a horizontal plane (a flat-Earth representation). Thus the x axis in our two-dimensional representation is the mean sea surface, and range information along the propagation path is measured in this coordinate. The z axis represents the vertical offset with $z = 0$ at mean sea level. The receiver location is specified by the coordinates $(0, z_r)$ and the transmitter is at (x_t, z_t).

A bundle of rays is defined at a common point at the receiver to span the vertical extent of the sensor field of view. Each ray is generated within the vertical plane containing the transmitter and receiver starting from the receiver location at $(0, z_r)$. If the source point is visible to the receiver, we can be certain that a fan of rays defined for launch angles $-\pi/2 < \theta < \pi/2$ will include rays that intercept the source. In practice, the computational angular extent of the fan of rays is further constrained because rays launched with a sharp downward angle will intercept the x axis (Earth surface) before the source range is achieved, or rays with a sharp upward launch angle will remain too high when extended to the source range.

In Fig. 11(a) we show an example of a ray computation. This example is typical of a subrefractive condition, and it was generated from a representative vertical refractive profile modeled during the experiment (day 322, 12:35 UT). Several unusual features can be noted in Fig. 11(a). There is a large disparity in length scales: The horizontal range is 16 km whereas the vertical height scale goes to 20 m. This causes any curvatures in the rays to appear much greater than they actually are. The full angular range of the fan of rays generated is only 1.2 mrad. Also, the effect of the flat-Earth coordinate transformation that equates the x axis with mean sea level can be seen: A straight line in the curved Earth frame appears as an upwardly curved arc with radius of curvature equal to the Earth radius.

In the example [Fig. 11(a)] two different rays are shown with heavier curves, corresponding to two viewing angles differing by 0.72 mrad, traced from the receiver point at range zero and height 8 m to the source point at range 15.7 km and height 10.7 m. This intersection at a downrange point of two rays with two different viewing angles is the signature of a mirage condition. The upper ray corresponds to an erect image, and a second lower ray corresponds to an inverted image. It is this type of refractive condition that generates the familiar pools of water seen on a hot flat stretch of highway pavement, apparently reflecting the sky or an other inverted image of an upper erect image.

The conditions for a subrefractive mirage require a surface temperature relatively warmer than the air temperature a short distance above the surface. Monin–Obukhov similarity theory can be applied to deduce the vertical temperature profile for this situation because the Richardson number is negative and unstable conditions apply. The form of the vertical temperature gradient given by similarity theory is

$$\frac{\mathrm{d}T}{\mathrm{d}z} \propto \ln\left(\frac{z}{z_0}\right), \tag{11}$$

where z is the height above the surface. Thus $\mathrm{d}T/\mathrm{d}z$ has a large negative value near the surface, and it increases toward zero as the height increases. For

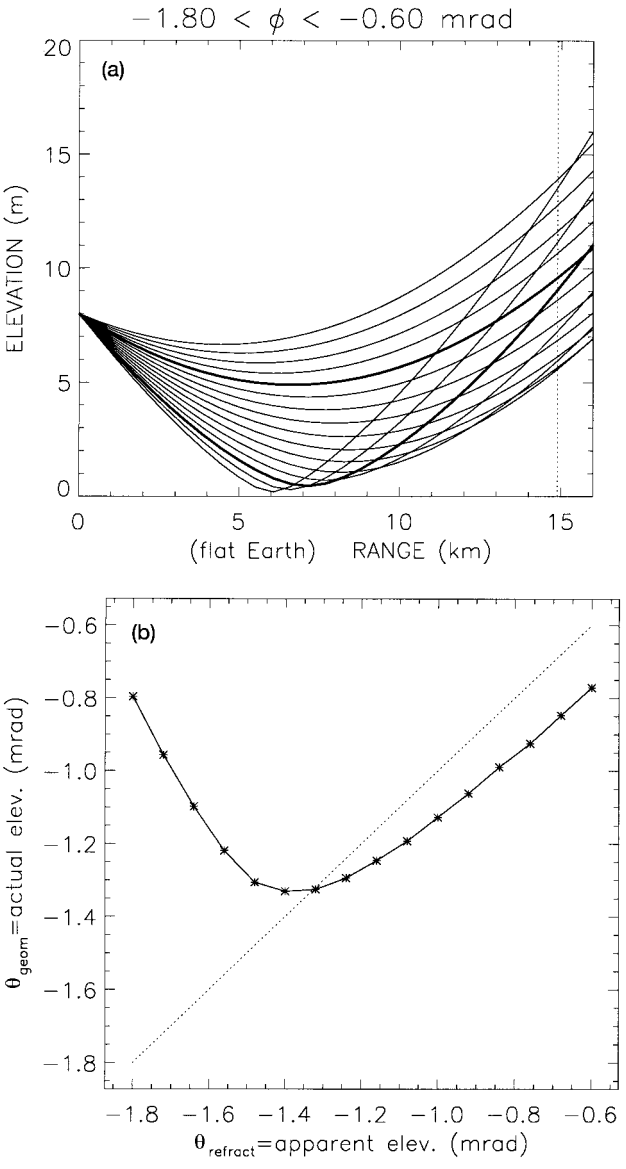

Fig. 11. (a) Ray trace computed for day 322, 12:35 UT. The ray trace is typical of a subrefractive condition in which an inferior mirage occurs. Note that the range is 16 km whereas the height is 20 m. Two different rays are shown with the heavier curves corresponding to the appearance of an erect image and an inverted mirage image of the point at range 15.7 km and height 10.7 m. (b) A transfer function for the ray trace shown in (a). The transfer function relationship is a map from the refractive apparent angular position ($\theta_{\mathrm{refract}}$) to the geometric atmosphere-free angular position (θ_{geom}).

optical and infrared frequencies, we can write the refractive index n as

$$n = 1 + \frac{C_0 p}{T}. \tag{12}$$

The pressure variations as a function of height can be neglected for our geometry, and hence

$$\frac{\mathrm{d}n}{\mathrm{d}z} = \frac{-C_0 P}{T^2}\frac{dT}{dz}. \tag{13}$$

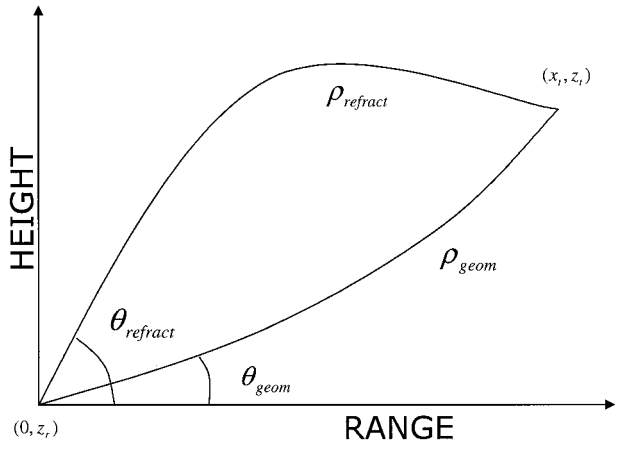

Fig. 12. Definition of a geometric ray and a refracted ray and the associated ray angles. There are two different rays between the receiver point and the transmitter point. The straight line ρ_{geom} is propagated in a free-space medium ($n \equiv 1$) and $\rho_{refract}$ corresponds to a ray in a medium with vertical refractivity gradients. The angles θ_{geom} and $\theta_{refract}$ are measured from the horizontal plane and the corresponding ray.

This shows that dn/dz is large and positive near the surface, and it decreases monotonically as z increases.

The implication for a ray calculation is that the radius of curvature decreases as the height above the surface decreases. This forces rays with more negative downward launch angles to enter regions generating an upward radius of curvature smaller than the ray above, and this in turn causes an intersection between the rays. Finally, this also imposes the conditions needed for a defined envelope for these rays, which is termed a caustic. In Fig. 11(a) the caustic is the envelope or fold boundary for the family of upward curving rays on the lower right portion of the ray trace.

The important features of the refractive conditions generating mirages are (i) the existence of a second distinct image of a source point, (ii) the orientation (erect versus inverted) of the image, and (iii) the distortion in the image. All this information is encoded within a functional dependence of elevation angles θ_{geom} ($\theta_{refract}$). The transfer function relationship is a map from the refractive apparent angular position ($\theta_{refract}$) to the geometric atmosphere-free angular position (θ_{geom}). A transfer function for the ray trace in Fig. 11(a) is shown in Fig. 11(b). The features (i), (ii), and (iii) above can all be determined from this function. The point at which this function has zero slope corresponds to the caustic point, and this point can also be located on the ray trace in Fig. 11(a) as the lowest height for all rays intersecting the vertical line at the 15-km range.

Our primary computational method for the determination of refractive effects within the propagation medium is portrayed by the geometry shown in Fig. 12. Figure 12 depicts a comparison between a single ray propagated in the refractive medium and the corresponding geometric reference ray. Note carefully that Fig. 12 is not a portrayal of the two rays involved in a mirage condition. There are two different rays that can be determined to propagate between $(0, z_t)$ and (x_t, z_t). A reference ray ρ_{geom} is propagated in a free-space medium ($n \equiv 1$) and hence it is a straight line. However, in our transformed flat-Earth coordinate system that takes the local spherical Earth surface to a flat plane, this free-space ray has the opposite curvature and the same radius of curvature as the Earth. The ray $\rho_{refract}$ corresponds to a ray propagated in a medium with vertical refractivity gradients, and hence it will usually define a curve. θ_{geom} measures the angle between ρ_{geom} and the horizontal plane, and $\theta_{refract}$ measures the angle between $\rho_{refract}$ and the horizontal plane. In a mirage condition, there can be a third ray defined between $(0, z_t)$ and (x_t, y_t).

Recall that the propagation factor F is the ratio between the actual field amplitude at a selected field point and the corresponding field amplitude at that point in free space ($n \equiv 1$). The field intensity at the receiver is given in terms of the field amplitude propagation factor F by

$$F^2 = \sum_{\theta_{refract}} \left| \frac{d\theta_{refract}/dz}{d\theta_{geom}/dz} \right|_{(x,z)=(x_t,z_t)}, \qquad (14)$$

where the summation is over all values $-\pi/2 < \theta_{refract} < \pi/2$ for which rays terminate at (x_t, z_t). The propagation factor is defined for horizontally homogeneous environments. This factor is dependent only on the spatial locations of the source point and receiver point in space. It is therefore necessary mathematically for the definition to include the full π-rad fan of rays for $\theta_{refract}$ to ensure that all rays from a source are accounted for at the receiver. Thus at the limiting angles, we have $\theta_{refract} = \theta_{geom} = \pi/2$ and $\theta_{refract} = \theta_{geom} = -\pi/2$ because it is only the vertical rays that are certain to be undeviated in a horizontally homogeneous refractive environment. Of course, in practice, the field of view of the sensor is clearly critical to the measurement of signal intensity, and it is clearly important that the mean pointing direction and the field of view be carefully adjusted to accommodate all rays (direct as well as mirage) that terminate at the sensor. Although the necessity of this is obvious, it should be noted that the practical implementation can be somewhat tricky. We noted above that our narrow field-of-view receiver telescope caused signal loss when the refractive conditions changed sufficiently to cause the beam to miss our receiver entirely during certain periods.

It is common to have subrefractive conditions that create inferior mirages; these conditions can occur whenever the air–sea temperature difference is negative ($T_{air} - T_{sea} \leq 0$). We subsequently show that these inferior mirage conditions are responsible for nearly all the occurrences of propagation factors larger than 1.05 in this field experiment.

It is possible for the refractive propagation factor F defined in Eq. (14) to become infinite. This occurs when the point (x_t, z_t) coincides with a caustic surface.

There are methods to resolve these singularities and determine the field intensity at a caustic.[30,31] For the point (x_t, z_t) to actually coincide with the caustic is a probability zero event, but fields can become quite large in the neighborhood of the caustic. For our model, it suffices to simply place an upper bound on the calculated factor.

For each field observation, a gain versus height calculation is made. The resulting gain curves are sensitive to small changes in elevation in some conditions, and some of the resulting difficulties are discussed below. Field variations over the vertical extent of our aperture (20 cm in diameter) were not considered in our calculations.

There are two primary requirements for the geometric ray-trace model to generate a signal-level prediction. First, the vertical refractive field is needed, and second the local geometry must be specified. The vertical displacement above sea level of both the transmitter and the receiver varied as a function of tide height. This changes the geometry of the ray-trace calculation and in some cases meant that the source disappeared below the apparent horizon.

Estimating the absolute error in the refractive analysis is rather complex. The refractive gradients generated by the LKB model depend not only on the air–sea temperature difference but also on wind speed and atmospheric pressure. A large number of events were omitted from the data analysis because of the failure of the LKB model to adequately determine a valid refractivity profile. Most of the events with a large positive air–sea temperature difference ($T_{\mathrm{air}} - T_{\mathrm{sea}} > 0$) are in this omitted category. The failure of the LKB model is by no means a new result: It is well known that many duct models fail for high air–sea temperature differences.

Furthermore, the rays entering the receiver are quite sensitive to transmitter and receiver altitude; hence they are quite sensitive to the tide.[32] This is especially true when the receiver is near a caustic. Small changes in either of these quantities affect the proximity of measurement point and cusp location. This problem is shown in Fig. 13. When the model places the location of the transmitter at point A in Fig. 13, the predicted propagation factor is either zero or close to zero. On the other hand, if the transmitter is located some 50 cm higher, say at point B, the propagation factor is quite large, with $F^2 > 10$. This sensitivity to transmitter height can cause estimates to be dramatically different from the observed signal intensity. A small number of errors of this magnitude can cause a substantial increase in the root-mean-square (rms) error measurement $\varepsilon_{\mathrm{rms}}$.

There are two further points to note in any error analysis of the τ model (transmission) and the σ model (signal). The first error is due to what can be called the temporal registration problem. As noted at the beginning of Section 5, statistically significant samples of the larger aerosol particles require longer averaging periods. Therefore the field data collection and averaging protocols resulted in both meteorological data and infrared data measurements every

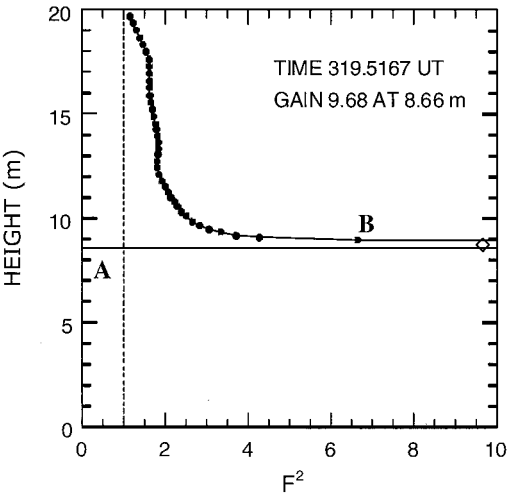

Fig. 13. Height versus gain calculation that shows the sensitivity of the calculation to small changes in transmitter height. At point A at an 8-m height, the propagation factor is zero, whereas at point B at a 9-m height, the propagation factor is $F^2 > 6.0$. The vertical dashed line represents the free-space signal level.

10 min, and the recording computers were synchronized only within several minutes. In this field data it is impossible to align the data collection events more accurately than a 10-min window. We know that both meteorological conditions and infrared transmission conditions can change substantially from one minute to the next.

A second source of error can cause the comparison of the τ and the σ models to be misleading. As Eq. (1) shows, each factor contributing to σ enters in a multiplicative way. In performing a comparison of the relative improvement induced by a refractive propagation factor, we implicitly assumed that the extinction calculations embodied in the τ model are accurate and that any errors in the calculations are random. This is false. We could in fact have a refractive propagation factor calculation that is perfect and still find that the rms error ($\varepsilon_{\mathrm{rms}}$) for σ is larger than $\varepsilon_{\mathrm{rms}}$ for τ.

Ignoring everything except the dependence of the LKB profiles on air and sea temperature, we estimated the error in F^2 by calculating the change in F^2 that is due to the changes in air and sea temperature from their mean value. The mean values were changed by an amount equal to the rms error in air and sea temperature between the two buoys. This resulted in the entries in the third row of Table 5.

C. Reflection Model

Only rays from direct and mirage families were used to compute the propagation factor. Reflected ray families were not used because the grazing optical reflectivity of a water surface roughened by capillary waves is low. This reflectivity Γ can be determined analytically[33]; and because Γ is less than 0.1% for all wind speeds we encountered, we ignored reflections altogether.

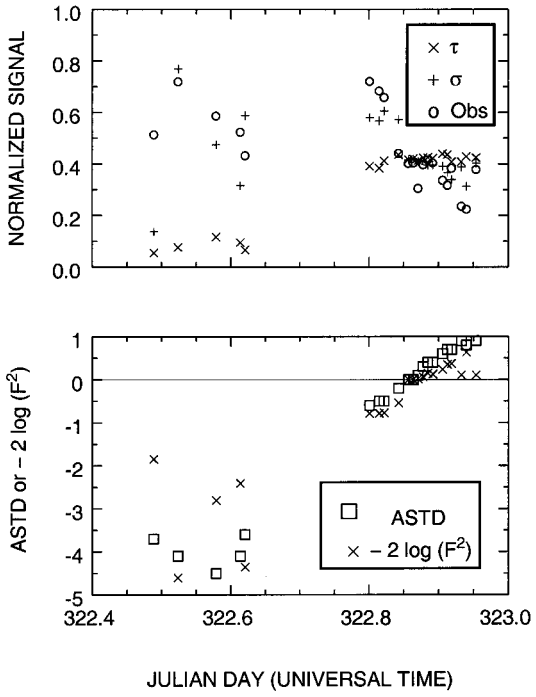

Fig. 14. Sequence of observations for the midwave band over an 11-h period is shown as open circles. Two predictions are compared: transmission τ and the refractive propagation correction σ. For the upper panel, the rms error for transmission prediction is 0.27 whereas the rms error for the signal with refractive correction is 0.12. ASTD, air–sea temperature difference.

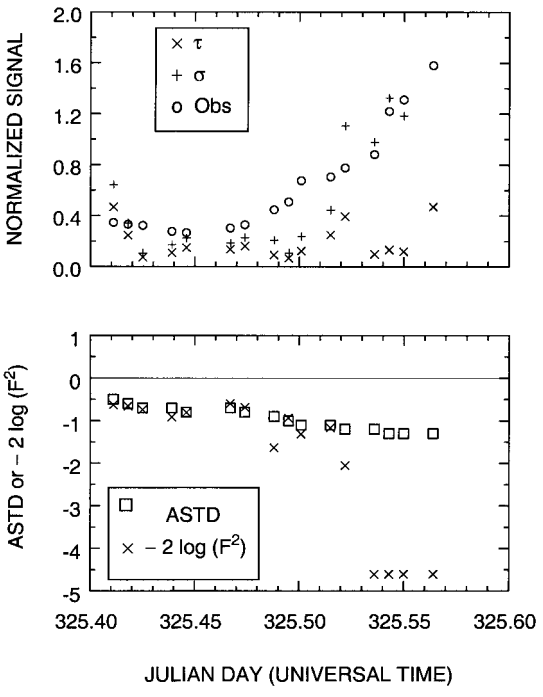

Fig. 15. Sequence of field observations for the midwave band over a 4-h, period that culminates with the signal exceeding the free-space value. For the interval shown, we find that the transmission rms error is 0.57, whereas the signal with refractive correction has a rms error of 0.79. The refractively corrected point at the right end of the sequence is shown with a value of 2, but the actual value was somewhat larger than 2. ASTD, air–sea temperature difference.

8. Signal Results

We now discuss the test of our model against the observed signal. Propagation factors were calculated for all time intervals for which both validated transmission measurements and the required meteorological data were available. The propagation factors were combined with the transmission calculations according to Eq. (1) and compared with the observed signal.

Inclusion of a refractive effects factor notably improved the calculated signal for some of the time periods. We examine two subintervals of the time series in Fig. 14. The upper panel in Fig. 14 shows a time-series interval for which $\tau = \tau_a\tau_m$ initially severely underestimates the observed values. At the right end of the interval, this has changed to an overestimate of the signal.

The lower panel in Fig. 14 displays $T_{\text{air}} - T_{\text{sea}}$ for the same time period as square symbols. Note that $T_{\text{air}} - T_{\text{sea}}$ is initially strongly negative, and by the end of the interval it becomes positive. Also plotted is $-2\log(F^2)$ where F is the propagation factor. It is clear that both quantities are strongly correlated, and both become positive at the same time. The importance of this transition can be seen in the upper panel of Fig. 15; $-2\log(F^2) > 0$ implies that $F^2 < 1.0$, and the values of τ, which are at this point overestimating σ, are corrected in the proper direction.

In the upper panel of Fig. 15, we consider a data sequence containing one of the events that motivated our study of refractive effects for this data. For $t \geq 325.55$ the observed signal exceeds the free-space value, and at the end of the sequence the observed signal is more than 1.5 times the free space value. Clearly τ is doing a poor job of predicting these larger signal values. The propagation factor clearly moves the prediction in the right direction, closer to the observed data. The exception to this useful correction trend occurs at the rightmost two data points. The refractively corrected points are shown at the upper edge of the plot bounding box: They have values larger than 2.0. This occurs because our refractive correction factor corresponds to a point near a caustic in the geometric ray envelope. There were several sustained time periods where the measured transmission exceeded the clear-air (aerosol-free, molecular extinction only) results, even exceeding free space (refractive index is unity) on several occasions for the midwave band.

The most stringent test of the efficacy of a model is to measure the pointwise error. Table 6 lists the rms error (ε_{rms}) and standard error (ε_{std}) along with several other statistics for each wave band. N gives the number of data points considered for each calculation. Statistics pertaining to a comparison between observations and calculations of clear-air transmission (based on the effects of molecules alone) are given in the rows labeled τ_m. Statistics pertaining to a comparison between observations and calcu-

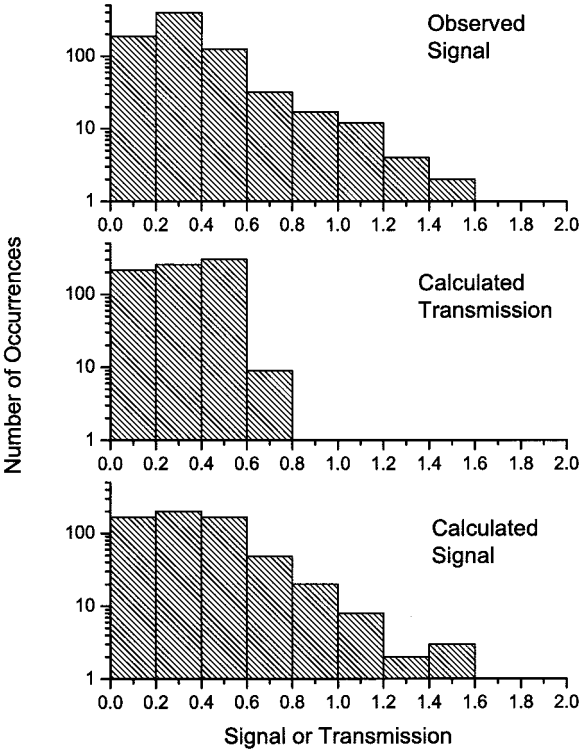

Fig. 16. Frequency distribution for the midwave observed signal, calculated transmission, and calculated signal, plotted on a logarithmic scale. The calculated signal σ is a better fit to the data than the calculated transmission τ.

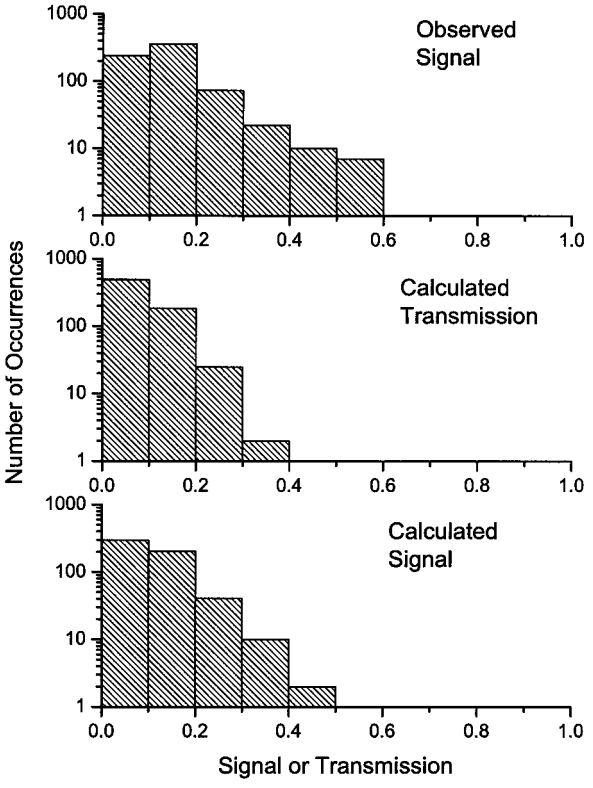

Fig. 17. Frequency distribution for the long-wave observed signal, calculated transmission, and calculated signal, plotted on a logarithmic scale.

lations of transmission (based on the effects of molecules and particles together) are given in the rows labeled τ. Statistics pertaining to a comparison between observations and calculations of signal (based on the effects of molecules, particles, and refraction) are given in the rows labeled σ.

In the statistics of Table 6, the rms error is perhaps the most informative measure to gauge the performance of our model.[20] Statistically, however, there is only a small reduction in the rms error when refractive effects are added to the effects of extinction. In the long-wave band, not only is the rms error reduced for σ, but the bias is also reduced when compared with τ. However, the same cannot be said for the midwave band. Although we did get a slight improvement in the rms error for σ in the midwave, calculations including refractive effects were more negatively biased than estimates without refraction. The midwave measurements also show a larger variance for σ than for τ.

In spite of these results, it is our contention that the inclusion of a propagation factor derived from refractive effects is a necessary component of any successful model. In Fig. 16 we show the frequency distributions for the observed signal, the calculated transmission τ, and the calculated signal σ for the midwave band and over the entire data set. Transmission calculations for the entire midwave data set reveal that $\tau < 0.7$, and this is shown by the distribution in the middle panel of Fig. 16. But the observed field signal in the top panel looks quite different because there are numerous occurrences greater than 0.8. We call these events high-intensity events. The calculated signal is shown in the bottom panel, and it is clear that the high-intensity events are captured by the signal calculation σ when we use the refractive propagation factor. This shows that, in a frequency distribution sense, the signal calculation σ is a better fit to the observations than the transmission calculation τ. A similar comparison for the long-wave band is shown in Fig. 17.

A primary result from the refractive analysis of the data is the correlation of the propagation factor F with $T_{\mathrm{air}} - T_{\mathrm{sea}}$. In Fig. 18 we show the propagation factor F_{cal} derived from model calculations plotted against $T_{\mathrm{air}} - T_{\mathrm{sea}}$. Note in particular that all calculated points are entirely within the quadrants 2 and 4: For $T_{\mathrm{air}} - T_{\mathrm{sea}} \leq 0$, we have $F_{\mathrm{cal}} \geq 1.0$, and for $T_{\mathrm{air}} - T_{\mathrm{sea}} \geq 0$, $F_{\mathrm{cal}} \leq 1.0$. This trend is an important indication of the correlation between the two quantities.

As indicated by Eq. (1), the propagation factor enters the signal calculation in a multiplicative way, and thus it is more effective to examine the propagation factor on a logarithmic scale. We find the cross correlation $P_{\Delta,\Phi_{\mathrm{cal}}}(0) = 0.77$ for the sample sets $\Delta = T_{\mathrm{air}} - T_{\mathrm{sea}}$ and $\Phi_{\mathrm{cal}} = -\log F_{\mathrm{cal}}$. In Fig. 18 the red crosses are plotted against the measured $T_{\mathrm{air}} - T_{\mathrm{sea}}$ (air–sea temperature difference). To confirm this trend for the measured data, for each value of $T_{\mathrm{air}} - T_{\mathrm{sea}}$ (measured to 0.1°C)

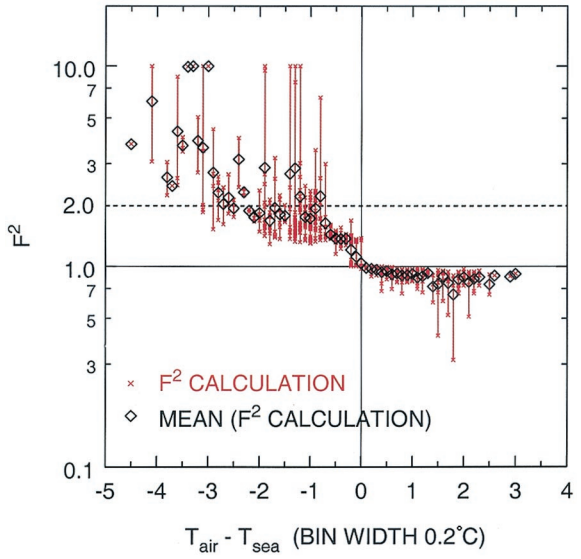

Fig. 18. Cross correlation between $T_{air} - T_{sea}$ and $F_{cal}{}^2$, shown for the entire midwave data set. The diamonds show the mean value of F^2 calculated for each temperature difference bin of width 0.1, $-4.5 \le T_{air} - T_{sea} \le 3.0$. Note in particular that $T_{air} - T_{sea} \le 0$ implies that $F_{cal} \ge 1.0$, and $T_{air} - T_{sea} \ge 0$ implies $F_{cal} \le 1.0$.

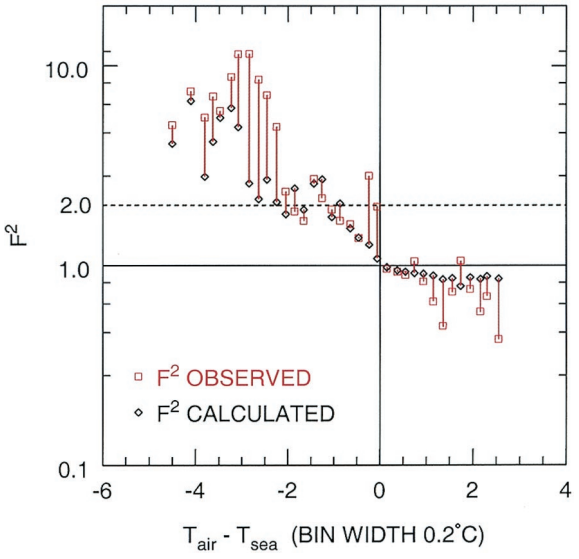

Fig. 19. Derived propagation factor F_{obs} for the midwave infrared signal intensity data from the entire experiment is directly compared with the propagation factor F_{cal} from the refractive effects model. Only the mean value for each $T_{air} - T_{sea}$ bin is shown. The cross correlation between averaged values of $\overline{F_{obs}{}^2}$ and $\overline{F_{cal}{}^2}$ is $P = 0.88$.

we calculate the mean value $\bar{F}_{cal}{}^2(T_{air} - T_{sea})$. These data are presented in the plot for each value of $T_{air} - T_{sea}$, $-4.5 \le (T_{air} - T_{sea}) \le 3.0$, and the results are shown as diamonds in Fig. 18.

To elucidate the correlation further, we discuss a second notable feature of the plot. The points for which $F_{cal}{}^2 \ge 1.0$ appear substantially separated from the line $F_{cal}{}^2 = 1.0$. There is a simple reason for this: For 99% of the points in this region, the ray optics model generated two separate ray solutions. Thus, for points in this region, an augmented intensity at the receiver is due to both a primary ray and a mirage ray solution. The occurrence of a second mirage ray does not necessarily double the received intensity. However, for almost all cases the transition from one ray to two rays does induce a discontinuous increase in received intensity.

We now examine the field data for a similar correlation. In Fig. 19 the midwave infrared signal intensity data from the entire experiment is directly compared with the refractive effects model. Recall from Eq. (1) that the variations in signal intensity are generated by a product of individual factors. When we use the logarithm of the signal, the contribution of individual factors becomes an additive process, and thus we examine the logarithm of the field-measured signal. Because the contribution from molecular extinction and aerosol extinction was determined for each point, we can divide these factors from the full signal and generate an effective observed propagation factor F defined by $F_{obs}{}^2 = \sigma/\tau$. The cross correlation is $P_{\Delta,\Phi_{cal}}(0) = 0.58$ for the sample sets $\Delta = T_{air} - T_{sea}$ and $\Phi_{obs} = -\log F_{obs}$ associated with the effective field propagation factor F_{obs}.

We simplified the data for Fig. 19 by showing simply the mean value for each $T_{air} - T_{sea}$ bin. The correlation between $T_{air} - T_{sea}$ and the propagation factor is apparent, and the trend is explained when we overplot the mean value for the same bins for the calculated propagation factor ($F_{cal}{}^2$). These mean values $\bar{F}^2{}_{obs}$ conform well to the relation exhibited for the calculated propagation factors. The cross correlation is $P_{\Phi_{cal},\Phi_{obs}}(0) = 0.88$ for the sample sets $\Phi_{cal} = -\log F_{cal}$ and $\Phi_{obs} = -\log F_{obs}$.

9. Conclusions

We have presented an analysis of infrared transmission data collected over a 15-day period in November 1996. This experimental data set was selected in part because of the occurrence of several different weather conditions over the span of the test. The early portion of the test was dominated by an unusual condition known as a Santa Ana, during which hot air over land is advected out to sea. Air–sea temperature differences ($T_{air} - T_{sea}$) as large as +10°C were recorded during this period.

A second feature of this particular field data set that warranted attention is the appearance of signal values well in excess of free-space levels for extended periods of time (30 min or more). To identify the reason for these high signals, we calculated all the contributing factors in the signal transmission process. The extinction that is due to absorption and scattering was calculated with MODTRAN for molecular extinction, and particle extinction was estimated by application of Mie theory to the continuous particle size distributions measured at one endpoint of the transmission path.

In our analysis, we show that, although the estimates of signal intensity provided by the transmis-

sion modulation factors described above are useful and necessary, they are also often poor estimations of the actual observed signal. It is our thesis in this paper that the necessary final component in a complete model for near-sea-surface infrared transmission is the propagation factor induced by refractive effects. The analysis in Table 6 showed that the inclusion of the refractive propagation factor to define the calculated signal σ generated a modest improvement in the error ε_{rms}. It also shows that our model provides an unbiased estimate of the measured signal. For a total of 551 observations in the long-wave band, the bias was 0.03 and the rms error was 0.08. For a total of 587 observations in the midwave band, the bias was -0.06 and the rms error was 0.23.

We have presented a refractive effects model that demonstrates that a refractive propagation factor is a critical component of an accurate transmission model within the marine surface layer. The propagation factor F is a multiplicative quantity that is derived entirely from the local refractive field and the geometry of the entire transmission system. Furthermore, the correlation that we showed between the calculated propagation factor F_{cal} and the observed effective propagation factor F_{obs} implies that F is a first-order term in a complete transmission model for near-surface horizontal paths.

Scott Sandgathe and Ronald Ferek of the U.S. Office of Naval Research supported the EOPACE field campaign. Douglas Jensen of Space and Naval Warfare Systems Center organized the EOPACE campaign. The Netherlands Ministry of Defence (assignment A95KM729) and the U.S. Office of Naval Research (grant N00014-96-1-0581) financed the participation of TNO-FEL in EOPACE. We acknowledge the support of our colleagues at TNO-FEL: Peter Fritz for his support in the transmission measurements and Alexander van Eijk for his support with MODTRAN and Mie calculations. We also thank Keith Jones and Tamar Neta for assistance in obtaining the buoy data and Mary Jordan for assistance in the meteorological analysis.

References and Notes

1. G. B. Matthews, B. E. Williams, A. Akkerman, J. Rosenthal, and R. de Violini, "Atmospheric transmission and supporting meteorology in the marine environment at San Nicolas Island," Tech. Rep. TP-79-19 (Pacific Missile Test Center, Pt. Mugu, Calif., 1978).
2. G. B. Matthews, "Comparisons of atmospheric transmittance and visibility data collected at San Nicolas Island during the May 1979 OSP/EOMET high mode operation," Tech. Rep. TP-82-16 (Pacific Missile Test Center, Pt. Mugu, Calif., 1982).
3. S. G. Gathman, "Optical properties of the marine aerosol as predicted by the Navy Aerosol Model," Opt. Eng. **22,** 57–62 (1983).
4. D. E. Kerr, *Propagation of Short Radio Waves* (McGraw-Hill, New York, 1951).
5. D. R. Jensen, S. G. Gathman, C. R. Zeisse, C. P. McGrath, G. de Leeuw, M. H. Smith, and P. A. Frederickson, "Electro-optical propagation assessment in coastal environments (EOPACE) overview and initial accomplishments," Opt. Eng. **40,** 1486–1498 (2001).
6. All times in this paper are in universal time.
7. One of the parameters required by the Navy Aerosol Model is derived from radon activity.
8. A. N. de Jong and P. J. Fritz, "EOPACE transmission experiments spring 1996; preliminary results," Tech. Rep. FEL-96-A090 (TNO Physics and Electronics Laboratory, The Hague, The Netherlands, 1997), pp. 1–46.
9. A. N. de Jong, P. J. Fritz, M. M. Moerman, and M. J. J. Roos, "Transmission experiments during EOPACE, November 1996 and August/September 1997; preliminary results," Tech. Rep. FEL-96-A269 (TNO Physics and Electronics Laboratory, The Hague, The Netherlands, 1998), p. 13 ff.
10. H. U. Sverdrup, M. W. Johnson, and R. H. Fleming, *The Oceans, Their Physics, Chemistry, and General Biology* (Prentice-Hall, Englewood Cliffs, N. J., 1942), p. 128.
11. C. R. Zeisse, B. D. Nener, and R. V. Dewees, "Measurement of low-altitude infrared propagation," Appl. Opt. **39,** 873–886 (2000), Fig. 4.
12. Models CSASP-200 and CSASP-100-HV, Particle Measuring Systems Inc., 5475 Airport Blvd., Boulder, Colo. 80301-2339.
13. S. G. Gathman, "The effects of the marine aerosol on infrared propagation over the world ocean," Oceanologia **41,** 489–513 (1999).
14. S. G. Gathman and M. H. Smith, "On the nature of surf generated aerosol and their effect on electro-optical systems," in *Propagation and Imaging through the Atmosphere*, L. R. Bisonnette and C. Dainty, eds., Proc. SPIE **3125,** 2–13 (1997).
15. G. de Leeuw, F. P. Neele, M. Hill, M. H. Smith, and E. Vignati, "Sea spray aerosol production by waves breaking in the surf zone," J. Geophys. Res. **105,** 29397–29409 (2000).
16. A. Berk, L. S. Bernstein, and D. C. Robertson, "MODTRAN: a moderate resolution model for LOWTRAN 7," Tech. Rep. GL-TR-89-0122 (U.S. Air Force Geophysics Laboratory, Hanscom Air Force Base, Mass., 1989).
17. F. X. Kneizys, E. P. Shettle, L. W. Abreu, J. H. Chetwynd, G. P. Anderson, W. O. Gallery, J. E. A. Selby, and S. A. Clough, "Users guide to LOWTRAN 7," Tech. Rep. AFGL-TR-88-0177 (U.S. Air Force Geophysics Laboratory, Hanscom Air Force Base, Mass., 1988).
18. G. Mie, "Beiträge zur Optik Trüber Medien, Speziell Kolloidaler Metallösungen," Ann. Phys. (Leipzig) **25,** 377–445 (1908).
19. E. Vignati, "Modelling interactions between aerosols and gaseous compounds in the polluted marine atmosphere," Tech. Rep. Risø-R-1163(EN) (Risø National Laboratory, Copenhagen, 1999).
20. L. T. Rogers, "Effects of variability of atmospheric refractivity on propagation estimates," IEEE Trans. Antennas Propag. **44,** 460–465 (1996).
21. G. de Leeuw, "Vertical profiles of giant particles close above the sea surface," Tellus Ser. B **38,** 51–61 (1986).
22. G. de Leeuw and C. W. Lamberts, "Influence of refractive index and particle size interval on Mie calculated backscatter and extinction," J. Aerosol Sci. **18,** 131–138 (1987).
23. F. E. Volz, "Infrared optical constants of ammonium sulfate, Sahara dust, volcanic pumice, and fly ash," Appl. Opt. **12,** 564–568 (1973).
24. E. P. Shettle and R. W. Fenn, "Models for the aerosols of the lower atmosphere and the effect of humidity variations on their optical properties," Tech. Rep. AFGL-TR-79-0214 (U.S. Air Force Geophysics Laboratory, Hanscom Air Force Base, Mass., 1977).
25. G. M. Hale and M. R. Query, "Optical constants of water in the 200-nm to 200-μm wavelength region," Appl. Opt. **12,** 555–563 (1973).
26. G. de Leeuw, "North-Sea project II. Aerosol measurements aboard a ship and calculated optical and infrared properties

of the marine atmosphere," Tech. Rep. PHL 1983-11 (Physics Laboratory TNO, The Hague, The Netherlands, 1983).
27. D. R. Jensen, R. Jeck, G. Trusty, and G. Schacher, "Intercomparison of Particle Measuring Systems, Inc.'s particle-size spectrometer," Opt. Eng. **22,** 746–752 (1983).
28. S. Hammel, "Sensitivity analysis for infrared propagation," Tech. Rep. 2989 (Spawar Systems Center, San Diego, Calif, 1998), pp. 601–610.
29. W. T. Liu, K. B. Katsaros, and J. A. Businger, "Bulk parameterization of air-sea exchanges of heat and water vapor including the molecular constraints at the interface," J. Atmos. Sci. **36,** 1722–1735 (1979).
30. Y. A. Kravtsov and Y. I. Orlov, *Geometrical Optics of Inhomogeneous Media* (Springer-Verlag, New York, 1990).
31. Y. A. Kravtsov and Y. I. Orlov, *Caustics, Catastrophes and Wave Fields* (Springer, New York, 1998).
32. Compare Ref. 11 and Figs. 5 and 6. The data for these two figures were obtained during our November 1996 experiment but have not been included in the present paper because they occurred during the power outage at the Imperial Beach Pier.
33. C. R. Zeisse, "Grazing reflectivity of the wind-ruffled sea," Tech. Rep. 1843 (Space and Naval Warfare Systems Center, San Diego, Calif., 2000).